

The impact of external gas accretion on the distribution of HI gas in galaxies

QIANHAN ZHANG ,^{1,2} MIN BAO ,^{1,2,*} YANMEI CHEN ,^{1,2,†} NIANKUN YU ,^{3,4,5} YONG SHI ,^{1,2}
 AND LUIS C. HO ,^{6,7}

¹*School of Astronomy and Space Science, Nanjing University, Nanjing 210023, China*

²*Key Laboratory of Modern Astronomy and Astrophysics, Nanjing University, Ministry of Education, Nanjing 210023, China*

³*Max Planck Institute for Radio Astronomy, Auf dem Hügel 69, 53121 Bonn, Germany*

⁴*National Astronomical Observatories, Chinese Academy of Sciences, Beijing, 100101, China*

⁵*Key Laboratory of Radio Astronomy and Technology, Chinese Academy of Sciences, Beijing, 100101, China*

⁶*Kavli Institute for Astronomy and Astrophysics, Peking University, Beijing 100871, China*

⁷*Department of Astronomy, School of Physics, Peking University, Beijing 100871, China*

ABSTRACT

Using the data from Mapping Nearby Galaxies at Apache Point Observatory (MaNGA) and HI-MaNGA surveys, we build a sample of 37 gas-star misaligned galaxies with robust HI detections, which are believed to have undergone external gas accretion processes. Both star-forming (SF) and quiescent (QS) misaligned galaxies exhibit narrower HI line widths compared to their gas-star aligned controls. The HI profiles of SF misaligned galaxies tend to be single-peaked, displaying a slightly higher fraction of single-peaked shape compared to their aligned controls. The QS misaligned galaxies exhibit prominently single-peaked HI profiles, while their aligned controls show distinct double-horned profiles. The shape of HI profiles is expected to change with the HI surface density radial gradients through external gas accretion — the interaction between the accreted gas and the pre-existing gas leads to the re-distribution of angular momentum and induces gas inflow. It suggests that the progenitors of SF misaligned galaxies are central HI-enriched, in this case, the shape of HI profiles is insensitive to the further increase of central HI surface density. The progenitors of QS misaligned galaxies are central HI-deficient, hence the transition from central HI-deficient to HI-enriched surface density leads to significantly more single-peaked HI profiles.

Keywords: Galaxy kinematics, Galaxy dynamics, Interstellar atomic gas

1. INTRODUCTION

According to conservation law of angular momentum (AM), stars ought to share the same direction of AM as gas if the evolution of a galaxy is dominated by internal processes. However, several decades ago, [Galletta \(1987\)](#) found the AM direction of the ionized gas and stellar disks being misaligned with each other in a SB0 galaxy NGC 4564. With the developments of long slit and integral

* Qianhan Zhang and Min Bao share first authorship.

† E-mail: chenym@nju.edu.cn.

field spectroscopic observations, galaxies with kinematically misaligned gas and stellar components (misaligned galaxies for short) were found to be common in the quiescent (QS) sequence with old stellar populations, in which the misaligned fraction stands 20%–50% (Sarzi et al. 2006; Davis et al. 2011; Barrera-Ballesteros et al. 2015). Meanwhile, this fraction turned out to be much lower (2%–5%) in the star-forming (SF) main sequence (Chen et al. 2016; Jin et al. 2016; Bryant et al. 2019).

The gas-star misaligned phenomenon is believed to originate from external processes, including gas accretion and/or galaxy mergers (Corsini 2014). L’Huillier et al. (2012) used a multi-zoom simulation based on TreeSPH code to analyze the mass assembly of 530 galaxies, revealing that smooth accretion dominates the assembly (77% of total mass), while mergers contribute obviously less (23%). Lagos et al. (2015) identified a similar trend in their simulations of QS misaligned galaxies: mergers alone produced misalignment in only 2% QS galaxies, while adding gas accretion processes increased this fraction to 46% — in good agreement with observational results. Furthermore, using the Mapping Nearby Galaxies at Apache Point Observatory (MaNGA) observations, Li et al. (2021) uncovered that the fraction of misaligned galaxies with merger remnant features exhibits insignificant increase compared to their control sample, illustrating that mergers are not the primary processes for the misaligned phenomenon. These results of simulations and observations support a consistent scenario that the formation of misaligned galaxies is dominated by external gas accretion.

Based on the MaNGA observations, Bao et al. (2025) found that the gas spins in misaligned galaxies tend to be perpendicular to the large-scale filaments, demonstrating that the misaligned gas is accreted from the large-scale structure. However, the impact of accretion on the gas content in misaligned galaxies is still not completely understood. On the one hand, gas accretion leads to an immediate increase in the gas content inside these galaxies. The collision between the pre-existing and accreted misaligned gas can redistribute angular momentum, and trigger gas inflow. On the other hand, the inflowing gas provides material for star formation and black hole activity in the galactic center (Lu et al. 2021). The feedback of these processes drives gas outflow, which can eventually reduces the gas content inside misaligned galaxies (Duckworth et al. 2020a,b). Through regulating the rates of gas inhalation and consumption, external gas accretion plays a critical role in the subsequent evolution of misaligned galaxies.

Previous studies found that the impact of gas accretion on the evolution of misaligned galaxies can be different in SF sequence and QS sequence. Based on a sample of SF misaligned galaxies selected from the early date release of MaNGA survey, both Chen et al. (2016) and Jin et al. (2016) found that the stellar populations in the central region of SF misaligned galaxies are younger than that in their outskirts, suggesting that the interaction between external accreted and pre-existing gas re-distributes the AM of gas component, leading to the gas inflow which triggers star formation in the central region. Different from SF misaligned galaxies, the stellar populations of QS misaligned galaxies show similar negative gradients as that of aligned controls, suggesting external gas accretion does not trigger the formation of new stars (Jin et al. 2016; Xu et al. 2022). Furthermore, Zhou et al. (2022) studied the global properties of the misaligned galaxies, finding larger asymmetry in ionized gas velocity fields in the misaligned galaxies than their aligned controls in both SF sequence and QS sequence. They also analyzed the HI detection rate and molecular gas mass fraction, finding that they are significantly lower in misaligned galaxies than their control samples in both sequences.

Cold gas, the fuel of star formation in galaxies, plays a critical role in galaxy evolution (Kennicutt & Evans 2012). 21 cm neutral hydrogen (HI) gas is one of the main components of cold gas, and it

has been proven to be a sensitive indicator of gas interactions due to its extended spatial distribution (Kornreich et al. 2000; Reichard et al. 2008; Wang et al. 2024). The extended HI disk can be easily distorted by external perturbation, such as tidal interaction, ram pressure stripping and gas accretion. Yun et al. (1994) discovered the interaction debris on M81 group through the spatially resolved HI observations, which is absent in their optical image. Although the single-dish observations are much cheaper than the spatially resolved ones, it still can provide plentiful information on the HI gas. For instance, the integrated flux of HI spectrum is a good indicator of HI gas mass, the line width and shape of HI spectrum can give clues on the spatial and velocity distribution of HI gas.

In this study, we build a sample of 37 misaligned galaxies with robust HI observations. By comparing their HI profiles with gas-star aligned control galaxies (aligned controls for short), we explore the impact of external gas accretion on the distribution of HI gas in galaxies. In Section 2, we introduce the data analysis and sample selection. We stack the HI spectra for misaligned galaxies and aligned controls, respectively, and make a comparison between them in Section 3. In Section 4, we quantify the difference in HI profiles between misaligned galaxies and aligned controls using the curve-of-growth (CoG) method. Based on these results, we discuss the impact of gas accretion in Section 5. Section 6 is the conclusion.

2. DATA AND SAMPLE SELECTION

2.1. *MaNGA survey*

MaNGA is one of the three core programs of the fourth generation of Sloan Digital Sky Survey (SDSS-IV; Bundy et al. 2015). It used the 2.5-m Sloan Foundation Telescope at Apache Point Observatory (Gunn et al. 2006) to observe 10,010 nearby galaxies (Abdurro’uf et al. 2022). These galaxies cover a flat distribution of stellar mass in $\log(M_*/M_\odot) \sim [9, 11]$, and redshift interval of $z \sim [0.01, 0.15]$ (Blanton et al. 2017). Two dual-channel BOSS spectrographs provide simultaneous wavelength coverage of [3600, 10,300] Å, which enable the measurements of all prominent emission lines from [O II] $\lambda\lambda 3726, 3729$ to [S II] $\lambda\lambda 6717, 6731$. The wavelength calibration accuracy is ~ 5 km s $^{-1}$. The spectral resolution is $R \sim 2000$.

The data products in the optical band are obtained from the final data release of MaNGA survey. The global properties of MaNGA galaxies in terms of stellar mass, redshift and photometric axial ratio in r-band ($q = b/a$) are obtained from the NASA-Sloan Atlas catalog (NSA¹, Blanton et al. 2011). The global stellar mass is estimated from spectral energy distribution (SED) fitting by the `kcorrect` package (Blanton & Roweis 2007) with BC03 single stellar population model (Bruzual & Charlot 2003) and Chabrier (2003) initial mass function. The axial ratio is converted into inclination angle following:

$$\sin i = \sqrt{\frac{1 - q^2}{1 - q_0^2}}, \quad (1)$$

where the intrinsic axial ratio (q_0) is set to be 0.2. Furthermore, the MaNGA Data Reduction Pipeline (DRP; Law et al. 2016) offers sky-subtracted and flux-calibrated 3D spectra. We stack the spectra with signal-to-noise (S/N) per pixel larger than 2, and measure the global 4000 Å break ($D_n 4000$) from the stacked spectrum of each galaxy. The MaNGA Data Analysis Pipeline (DAP; Westfall et al. 2019) offers measurements of spatially resolved properties, such as stellar and gas kinematics.

¹ <http://nsatlas.org>

2.2. *HI-MaNGA survey*

Hi-MaNGA² (Masters et al. 2019; Stark et al. 2021) is a follow-up survey of HI observations for the MaNGA galaxies with $z \leq 0.05$. The data products of HI spectra are obtained from the third data release of the HI-MaNGA value-added catalog, including the integrated HI flux (F_{HI}), flux-weighted central velocities (V_C) and W_{50} defined as the line width at 50% of the peak flux in the case of a single-peaked spectrum (or the maximum width at 50% of the peak flux on either side of a double-horned spectrum). In this catalog, 1147 galaxies are detected by Arecibo telescope (Haynes et al. 2018) with spectral resolution of $\sim 5.5 \text{ km s}^{-1}$, and 2030 galaxies are detected by Green Bank Telescope (GBT) with spectral resolution of $\sim 5 \text{ km s}^{-1}$.

Given the large beam size of Arecibo telescope ($\sim 3.5'$) and GBT ($\sim 9'$), the HI observations of MaNGA galaxies could be contaminated by companions. Witherspoon & Wilcots (2024) found that some active galactic nuclei (AGN) in low-mass galaxies with HI detection in the HI-MaNGA catalog are actually HI-poor, but contaminated by HI-rich companions. Stark et al. (2021) marked the potential contaminated sources located within 1.5 times the half-power beamwidth of the primary target and at a similar redshift. Additionally, they estimated the probability that more than 20% flux in this beam is contributed by companions ($P_{R>0.2}$), where R corresponds to the fraction of contribution to the total measured flux from the companions. Stark et al. (2021) suggested $P_{R>0.2} < 0.1$ as a criteria for selecting galaxies whose contamination of HI emission can be neglected.

2.3. *Sample selection*

Following the method of Zhou et al. (2022), we build a sample of 496 misaligned galaxies from the final data release of MaNGA survey. Firstly, we collect 7459 emission-line galaxies with the signal-to-noise ratios (S/N) of H α emission lines larger than 3 for at least 10% spaxels within $1.5 R_e$. Secondly, we fit the kinematic position angle for gas (PA_{gas}) and stellar (PA_{*}) components using Python-based code PAFIT (Krajnović et al. 2006). The position angle is defined as the counterclockwise angle between the north and the major axis of the velocity field on the receding side. The misaligned candidates are selected as $\Delta PA \equiv |PA_{\text{gas}} - PA_*| \geq 30^\circ$, and $PA_{\text{error}} \leq 20^\circ$ is required for robust position angle measurements, where PA_{error} is the 1σ error of PA. Finally, we visually inspect these candidates to remove ongoing mergers and galaxy pairs located within the same MaNGA bundle. Figure 1 displays an example of misaligned galaxies. Figure 1(a) shows the DESI image of g, r, z bands with the MaNGA bundle shown as a purple hexagon. Figures 1(b) and 1(c) display the stellar and gas velocity fields, respectively. The black dashed line marks the PA for the corresponding component, with PA values labeled in the top-left corner of each panel. It is clear that this is a counter-rotator with $\Delta PA \sim 180^\circ$ between stellar and gas components, an extreme subclass in gas-star misalignment.

We cross-match the misaligned sample with the HI-MaNGA value-added catalog (Stark et al. 2021), obtaining HI spectra for 102 misaligned galaxies. The S/N of each HI spectrum can be defined as

$$S/N = \frac{F_{HI}}{\sigma \delta V \sqrt{N_{chan}}}, \quad (2)$$

where σ is the root-mean-square (rms) of a spectrum, which represents the noise level (in unit of Jy), δV is the spectral resolution in unit of km s^{-1} , and N_{chan} is the channel number of spectrum. By

² <https://greenbankobservatory.org/science/gbt-surveys/hi-manga>

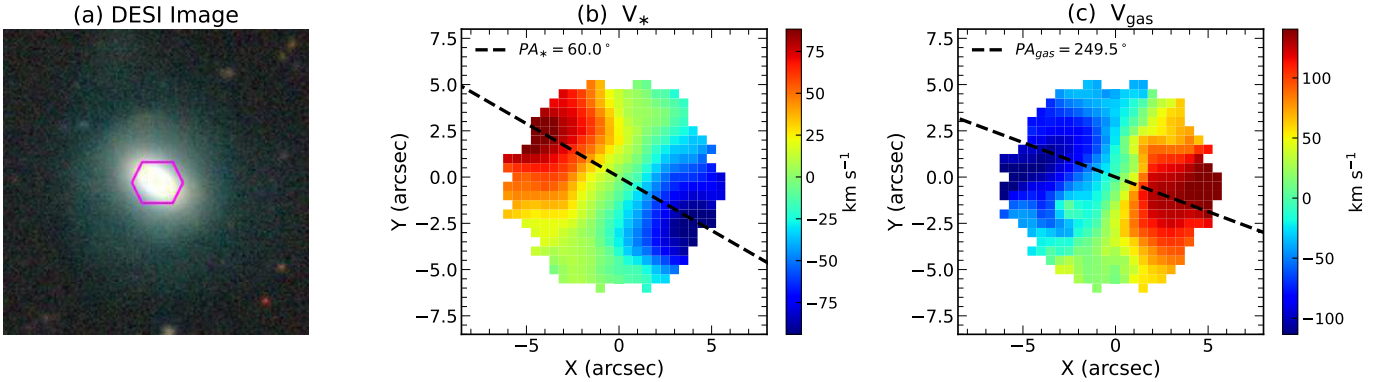


Figure 1. An example of misaligned galaxies MaNGA 1-418253. (a) The DESI g, r, z image. The purple hexagon shows the MaNGA bundle. (b) Stellar velocity field. The black dashed line shows the kinematic position angle the stellar disk. (c) Gas velocity field. The black dashed line shows the kinematic position angle of the gas disk. In panels (b) & (c), the blue and red colors represent velocities approaching and receding from the galactic center.

analyzing 10,000 mocked HI spectra with varying S/N, Yu et al. (2022) demonstrated that the statistic analysis of spectra with $S/N > 5$ is reliable. Therefore, we exclude 7 misaligned galaxies with HI spectral $S/N \leq 5$. Moreover, contamination from companions can lead to inaccurate measurements of HI profiles. We further exclude 58 misaligned galaxies whose HI emission is contaminated by companions as: (1) $W_{50} > 500 \text{ km s}^{-1}$ or (2) $P_{R>0.2} > 0.1$. Finally, a sample of 37 misaligned galaxies with robust HI observations is selected for the following studies. We list MaNGA-ID as well as some basic parameters of the 37 misaligned galaxies in the Table 1.

Figure 2(a) displays the galaxy distribution in a two-dimensional plane of global M_* and D_n4000 . D_n4000 is strongly correlated with the light-weighted stellar population age, and sensitive to star formation in \sim Gyr timescale. The black contour shows the distribution of 10,010 galaxies from SDSS DR17, which presents two density peaks. The peak at the bottom-left with lower M_* and D_n4000 corresponds to the SF sequence, while the peak at the top-right with higher M_* and D_n4000 corresponds to the QS sequence. To compare the impact of gas accretion on SF and QS galaxies, we classify the misaligned galaxies into SF sequence and QS sequence with a cutoff showed as black dashed line. The blue squares and red triangles show the distributions of 17 SF and 20 QS misaligned galaxies, respectively. We apply M_* - D_n4000 rather than M_* -SFR relation to separate SF sequence and QS sequence, because: (1) different from SFR, D_n4000 can be measured consistently for SF and QS galaxies; (2) the interaction between pre-existing and accreted external gas can lead to higher SFR in SF misaligned galaxies (Chen et al. 2016; Jin et al. 2016; Xu et al. 2022), while it has a smaller impact on D_n4000 which indicates star formation in \sim Gyr timescale.

2.4. Control sample

In order to understand the impact of external gas accretion on the distribution of HI gas, we build an aligned control sample with $\Delta PA < 30^\circ$, HI spectral S/N > 5 , $W_{50} < 500 \text{ km s}^{-1}$ and the contamination from companions can be neglected ($P_{R>0.2} < 0.1$). For each misaligned galaxy, one aligned control galaxy is closely matched in three dimensional parameter space of stellar mass ($|\Delta \log M_*| < 0.1$), 4000 Å break ($|\Delta D_n4000| < 0.05$) and inclination angle ($|\Delta i| < 10^\circ$). The motivation for choosing these parameters is: (1) stellar mass is the most fundamental property of a

Table 1. Misaligned galaxies with robust HI measurements

MaNGA-ID	Class	z	$\log(M_*/M_\odot)$	D_n4000	i (deg)	W_{50} (km/s)	S/N
(1)	(2)	(3)	(4)	(5)	(6)	(7)	(8)
1-137890	SF	0.027	9.58	1.34	58.51	174.55	18.50
1-138140	SF	0.047	10.18	1.52	30.29	138.48	7.77
1-199775	SF	0.030	9.91	1.37	41.11	114.55	7.58
1-547295	SF	0.041	9.53	1.38	45.59	105.59	11.41
1-38887	SF	0.024	9.31	1.35	61.65	165.08	9.84
1-207984	SF	0.038	9.55	1.40	37.89	187.68	16.25
1-246517	SF	0.019	9.15	1.42	55.01	147.06	11.68
1-94690	SF	0.031	9.91	1.57	60.66	292.68	10.10
1-272473	SF	0.044	9.97	1.48	66.56	NaN	10.39
1-51810	SF	0.021	9.72	1.45	22.63	142.08	42.89
1-153038	SF	0.018	9.10	1.20	32.89	70.96	10.69
1-109275	SF	0.044	9.73	1.39	49.78	218.69	12.94
1-153901	SF	0.040	9.70	1.33	48.04	124.59	8.68
1-24055	SF	0.030	9.32	1.40	55.64	78.66	9.81
1-118363	SF	0.026	9.57	1.41	70.95	NaN	13.53
1-587628	SF	0.019	9.73	1.16	28.11	NaN	18.47
1-386932	SF	0.026	9.56	1.32	51.00	NaN	5.88
1-339061	QS	0.020	10.00	1.61	53.37	336.72	25.11
1-338746	QS	0.032	10.16	1.77	26.78	153.24	7.40
1-235530	QS	0.027	10.00	1.82	26.96	239.09	15.64
1-93378	QS	0.049	10.26	1.85	36.00	230.07	9.63
1-94228	QS	0.049	10.28	1.88	30.80	36.58	5.14
1-561039	QS	0.026	9.97	1.68	71.04	195.44	26.36
1-178824	QS	0.013	9.45	1.62	55.27	45.62	9.24
1-180080	QS	0.030	10.28	1.71	31.78	496.26	18.31
1-38543	QS	0.023	10.05	1.77	58.19	313.24	6.50
1-71956	QS	0.040	9.54	1.58	32.81	82.24	9.86
1-456984	QS	0.018	10.86	1.98	21.89	NaN	8.36
1-174947	QS	0.033	10.37	1.75	60.20	400.39	17.77
1-188177	QS	0.027	9.98	1.61	43.73	164.21	22.45
1-246484	QS	0.030	9.41	1.66	54.02	158.37	9.82
1-462966	QS	0.032	10.48	1.89	47.52	253.48	14.23
1-153127	QS	0.018	9.49	1.73	37.68	298.95	55.02
1-189376	QS	0.019	9.56	1.65	33.11	105.78	6.33
1-319646	QS	0.029	9.96	1.70	64.66	122.42	17.80
1-152010	QS	0.028	9.40	1.56	47.37	149.40	7.00
1-198125	QS	0.036	10.12	1.93	43.38	378.41	9.81

(1) MaNGA-ID; (2) The classification of the galaxy using stellar mass and D_n4000 , including star-forming (SF) and quiescent (QS) sequence; (3) Redshift; (4) Stellar mass; (5) Global 4000Å break; (6) The inclination angle of the galaxy calculated through Equation 1; (7) Line width at 50% of the peak flux in the case of a single-peaked spectrum (or the maximum width at 50% of the peak flux on either side of a double-horned spectrum); (8) The signal-to-noise ratio of the HI spectrum.

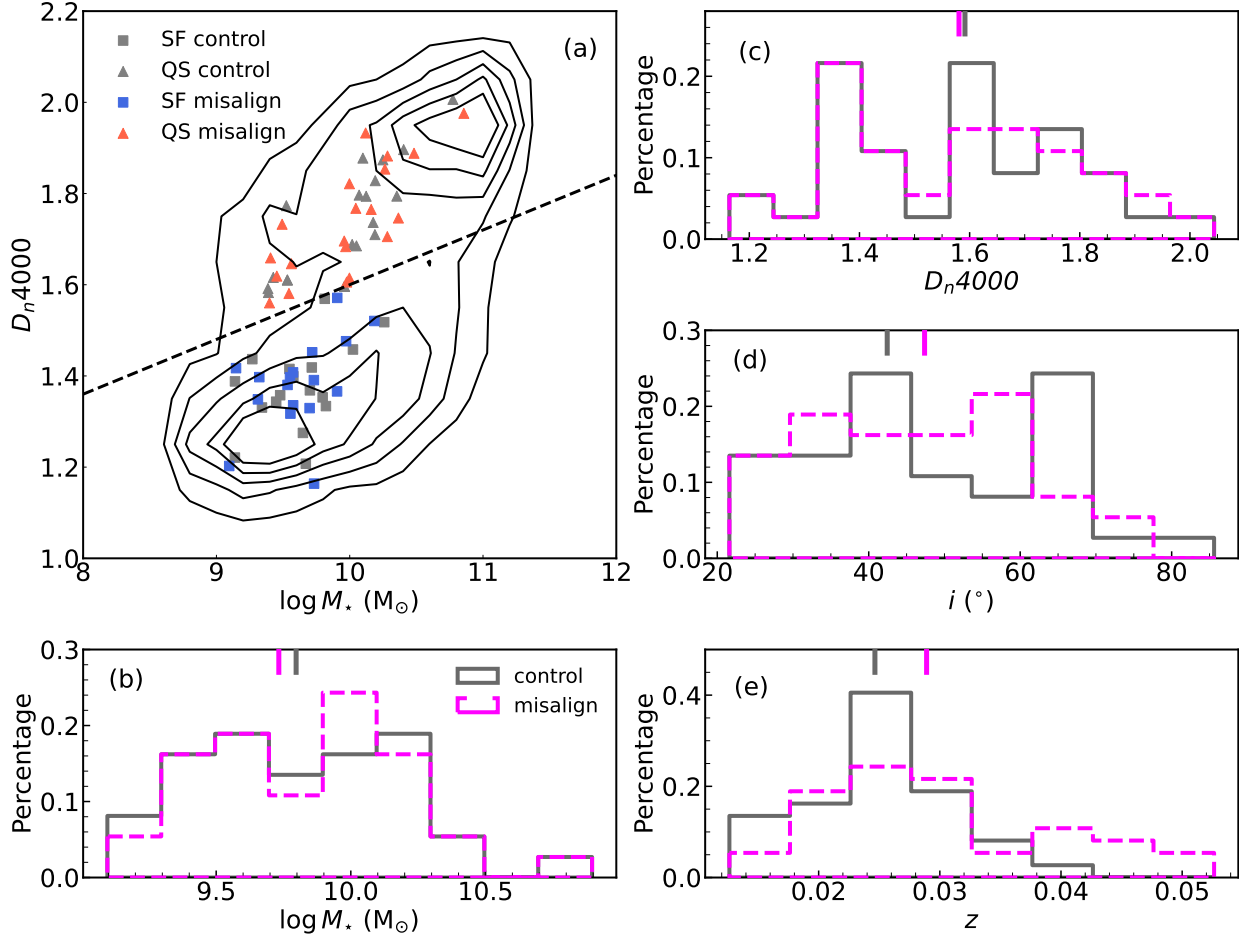


Figure 2. The physical properties of misaligned galaxies and aligned controls. (a) The galaxy distribution in a two-dimensional plane of M_* and D_n4000 . The black contour shows the distribution of SDSS galaxies. The black dashed line separates galaxies into SF sequence and QS sequence. The blue and gray squares represent SF misaligned galaxies and aligned controls. The red and gray triangles represent QS misaligned galaxies and aligned controls. (b) Stellar mass distribution. (c) D_n4000 distribution. (d) Inclination angle distribution. (e) Redshift distribution. In panels (b), (c), (d) and (e), the pink and gray histograms represent the distributions of misaligned galaxies and aligned controls, respectively. The pink and gray bars on the top show the corresponding median values.

galaxy, and it is tightly related to various other physical properties; (2) the similar global D_n4000 ensures that misaligned galaxies and aligned controls have similar stellar populations with comparable light-weighted ages averaged over the past few Gyrs; and (3) the inclination of a galaxy can affect the observed HI profile (El-Badry et al. 2018).

The gray squares in Figure 2(a) show the distribution of 17 SF aligned controls, and gray triangles show the distribution of 20 QS aligned controls. Figures 2(b), 2(c) and 2(d) display the distributions of $\log M_*$, D_n4000 , and i for misaligned galaxies (pink histogram) and their aligned controls (gray histogram), respectively. The pink and gray bars mark the median values for corresponding distributions. Figure 2(e) displays the distribution of z , color-coded in the same way as other panels. The difference in median redshifts between misaligned galaxies and aligned controls is less than 0.005.

3. INDIVIDUAL & STACKING HI PROFILES

To obtain an intuitive sense of the HI profiles in misaligned galaxies and their aligned controls, we first check the HI profile of each individual galaxy. Figure 3 show typical examples of HI profile, for each sub-sample (SF misalign vs. control, QS misalign vs. control), one single-peaked HI profile and one double-horned profile are provided. Each profile is normalized by its peak flux. Panels (a) and (b) show SF misaligned galaxies (blue) and their controls (gray). 11 out of 17 SF misaligned galaxies ($\sim 65\%$) exhibit single-peaked profiles, while the single-peaked fraction in SF control is $\sim 47\%$. Panels (c) and (d) show QS misaligned galaxies (red) and their controls (gray). 13 out of 20 QS misaligned galaxies (65%) show single-peaked profile, while the fraction in QS control is only 25%, which is 1.6 times lower than that of the QS misaligned galaxies.

We further compared the HI linewidth (W_{50}) of these galaxies. It should be noted that, 32 galaxies have reliable W_{50} measurements from HI-MaNGA catalog, while the others lack W_{50} measurement due to the non-smooth HI profile. Figure 4 displays the W_{50} distributions for these 32 misaligned galaxies and their aligned controls. Panel (a) shows SF misaligned galaxies (blue) and their controls (gray). It is significant that the misaligned galaxies exhibit narrower W_{50} compared with their aligned controls. Panel (b) shows QS misaligned galaxies (red) and their controls (gray) with the difference of W_{50} in QS sequences being more obvious than that in SF sequences.

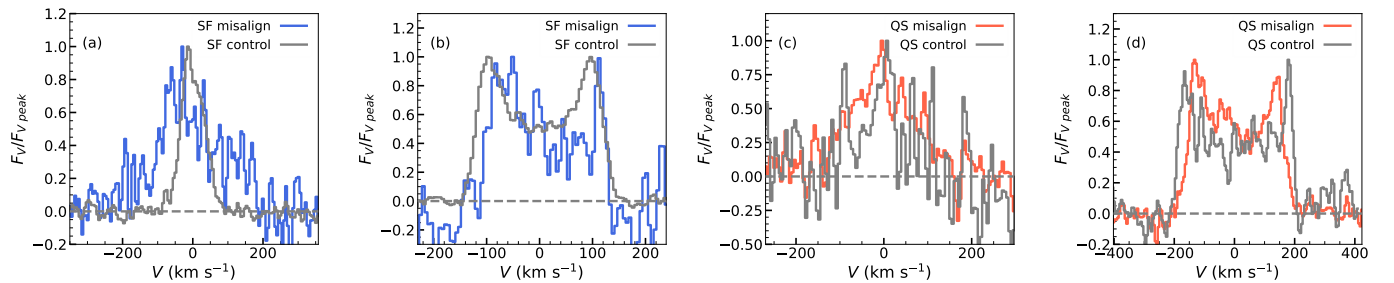


Figure 3. Examples of HI profiles. (a) Star-forming (SF) misaligned galaxy and aligned control with single-peaked HI profiles; (b) SF misaligned galaxy and aligned control with double-horned HI profiles; (c) Quiescent (QS) misaligned galaxy and aligned control with single-peaked HI profiles; (d) QS misaligned galaxy and aligned control with double-horned HI profiles. Blue (red) lines represent the SF (QS) misaligned galaxies and gray lines represent the aligned controls. Each profile is normalized by its peak flux.

In addition, to provide a clear, visual illustration of the characteristic differences in HI profiles between the misaligned galaxies and their controls, we compare the stacked HI spectra between them. The process of HI spectral stacking includes:

- (1) subtracting the systemic velocity V_C to shift each baseline-subtracted HI spectrum to the rest frame;
- (2) extracting each HI spectrum in a velocity range of $[-500, 500]$ km s $^{-1}$, and normalizing it by its peak flux;
- (3) adjusting the channel widths to 5 km s $^{-1}$ through linear interpolation;
- (4) ensuring that the integrated flux in $0 < V < 500$ km s $^{-1}$ is larger than that in $-500 < V < 0$ km s $^{-1}$, otherwise, mirroring the spectrum;
- (5) stacking the HI spectra following a weighting function:

$$S_{stack} = \frac{\sum_{i=0}^N S_i w_i}{\sum_{i=0}^N w_i} \quad (3)$$

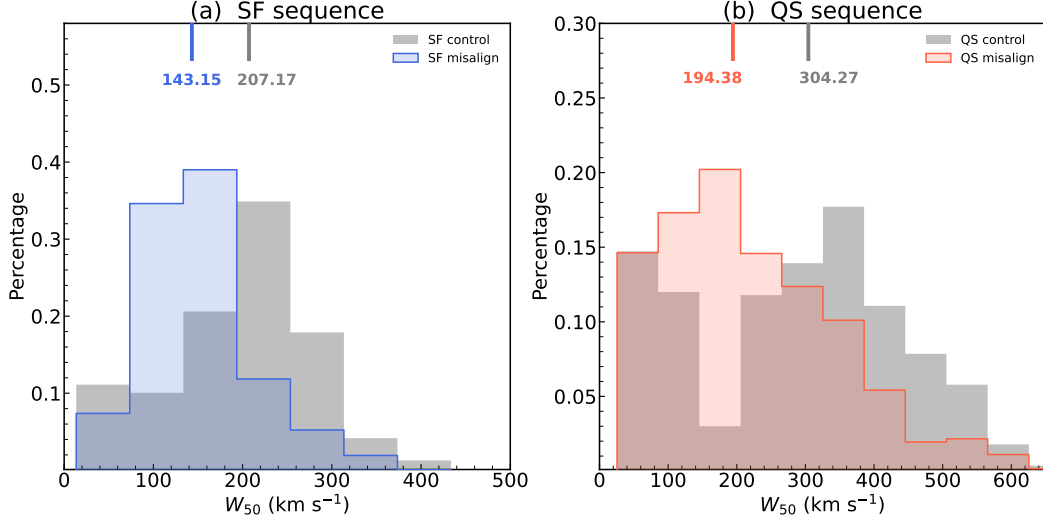


Figure 4. The distributions of line widths (W_{50}) for misaligned galaxies and aligned controls. (a) The blue and gray histograms show the line widths distribution for SF misaligned galaxies and their aligned controls, respectively. The blue and gray bars on the top mark the corresponding median values. (b) The red and gray histograms show the line widths distribution for QS misaligned galaxies and their aligned controls, respectively. The red and gray bars on the top mark the corresponding median values.

where S_i is HI spectrum of a galaxy after the preceding steps, $w_i = 1/rms_i^2$ is the corresponding weighting factor, where rms is the root mean square noise of the spectra (Fabello et al. 2012).

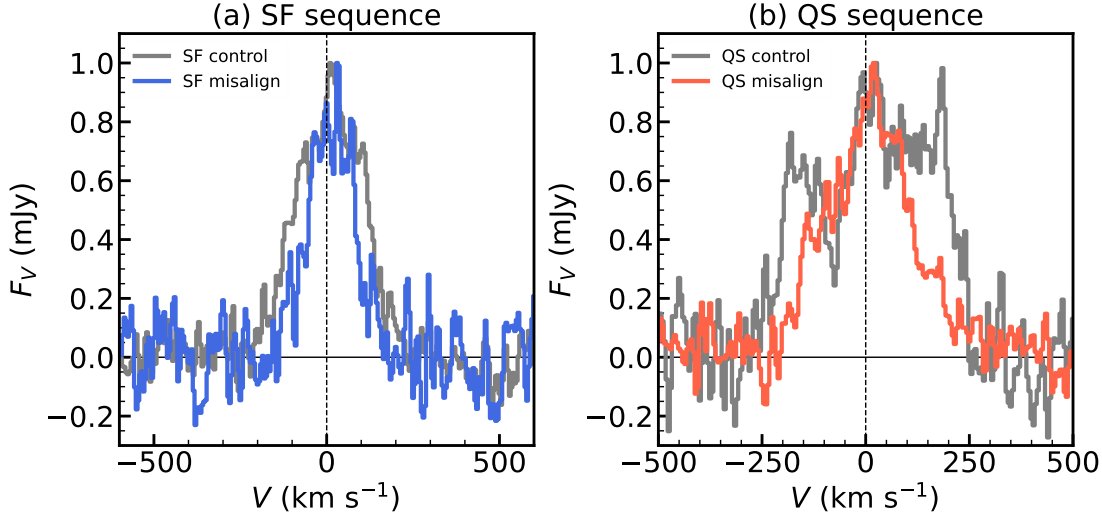


Figure 5. Stacked HI spectra in misaligned galaxies and aligned controls. (a) Blue and gray profiles show the stacked HI spectra in SF misaligned galaxies and their aligned controls, respectively. (b) Red and gray profiles show the stacked HI spectra in QS misaligned galaxies and their aligned controls, respectively. In panels (a) & (b), the vertical dashed line marks the position of $V = 0$ km s⁻¹, and the horizontal solid line marks the flux of $F_V = 0$ mJy.

Given the different impact of gas accretion on SF and QS misaligned galaxies, we stack the HI spectra in these sequences separately and make comparisons with corresponding aligned controls.

The blue and gray profiles in Figure 5(a) display the stacked HI spectra for SF misaligned galaxies and SF aligned controls. The vertical dashed line marks the position of $V = 0 \text{ km s}^{-1}$. The stacked HI spectrum in SF misaligned galaxies ($W_{50} \sim 130.5 \text{ km s}^{-1}$) is narrower than that in SF aligned controls ($W_{50} \sim 220.4 \text{ km s}^{-1}$).

The red and gray profiles in Figure 5(b) displays the stacked HI spectra for QS misaligned galaxies and QS aligned controls. The line width in QS misaligned galaxies ($W_{50} \sim 231.4 \text{ km s}^{-1}$) is obviously narrower than that in QS aligned controls ($W_{50} \sim 406.6 \text{ km s}^{-1}$). This tendency is consistent with SF sequence, while the difference is more prominent. As a result of the operation in step (4), all the stacked spectra have positive velocity at the position of peak flux ($V_{\text{peak}} > 0 \text{ km s}^{-1}$). To quantitatively compare the HI shape and asymmetry between misaligned galaxies and their aligned controls, we measure these parameters for the HI spectrum of each galaxy in the next section.

4. MEASUREMENTS OF HI PROFILE PARAMETERS

4.1. *CoG method*

To measure the shape and asymmetry of each HI spectrum, we apply the curve-of-growth(CoG) method developed by Yu et al. (2020, 2022). For each HI spectrum, we extract channels with flux higher than 0 mJy within the velocity range of $[-500, 500] \text{ km s}^{-1}$. The CoG is built through integrating flux as a function of velocity from line center ($V_C = 0 \text{ km s}^{-1}$) outward to both blueshifted and redshifted sides. The flux in blueshifted side is integrated within $V \sim [-500, 0] \text{ km s}^{-1}$ (F_B), while that in redshifted side is integrated within $V \sim [0, 500] \text{ km s}^{-1}$ (F_R). The A_F value indicating HI spectral asymmetry is defined as the larger value of F_B/F_R and F_R/F_B . Figure 6(a) displays two mock spectra, with blue and red colors representing the blueshifted and redshifted sides, respectively. The solid profile shows a symmetric HI spectrum, while the dashed profile shows an asymmetric HI spectrum. Figure 6(b) displays the CoG on each side of the two spectra, with colors and curves coded in the same way as Figure 6(a). The total CoG for the asymmetric HI spectrum (the dashed spectrum in Figure 6a) is defined as the sum of the integrated flux from the blue-shifted and red-shifted sides, as illustrated by the black dashed line in Figure 6(b). For the symmetric HI spectrum (solid spectrum in Figure 6a), the CoG is exactly the same for both blueshifted and redshifted sides (red solid line in Figure 6b). The A_F values for the two HI spectra are labeled in the top-left corner. In general, the higher A_F value corresponds to the higher HI asymmetry.

As shown in Figure 6(b), we take 85% and 25% of the flux at the flatten part of CoG as F_{85} and F_{25} , and define the corresponding velocity widths as V_{85} and V_{25} , the concentration of HI profile is characterized as $C_V = V_{85}/V_{25}$. Meanwhile, Yu et al. (2022) introduced a new parameter K to quantify the spectral shape. For each HI spectrum, the CoG is normalized by V_{85} along the velocity axis and by F_{85} along the flux axis. K is then calculated as the area between the normalized CoG and the diagonal line. Figure 6(c) displays three mock spectra, with the black, green and red profiles representing flat-topped, single-peaked and double-horned shapes, respectively. The black profile in Figure 6(d) shows the normalized CoG for flat-topped shape, which exactly follows the diagonal line ($K = 0$). The green profile in Figure 6(d) shows the normalized CoG for single-peaked spectral shape, and the light-green area marks the corresponding K value ($K = 0.1$). Similarly, the red profile and light-red area show the normalized CoG and absolute K value ($K = -0.2$) for double-horned spectral shape. The K value increasing from negative to positive corresponds for the HI spectral shape changing from double-horned to single-peaked.

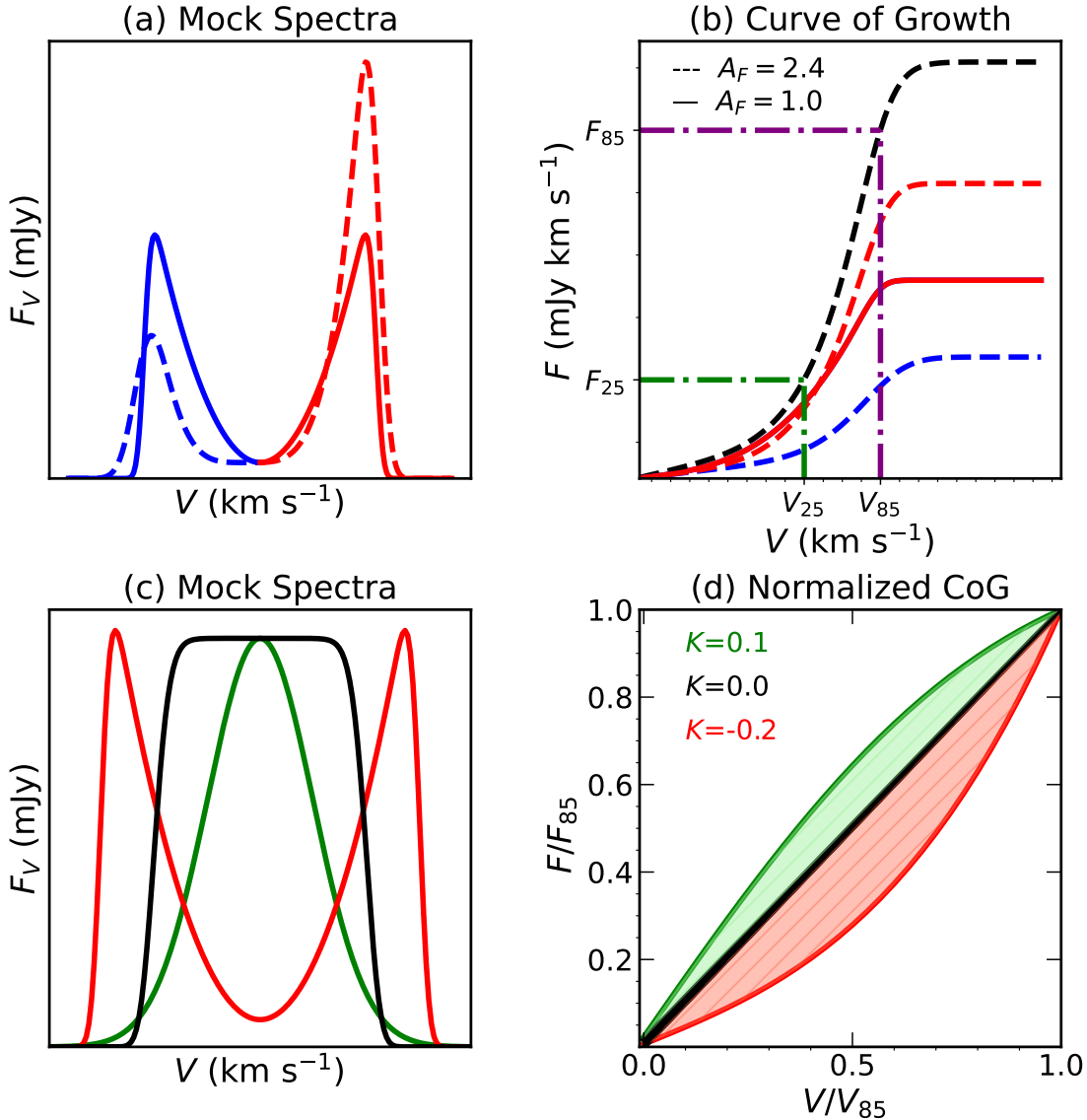


Figure 6. Schematic view to illustrate the CoG method. (a) Mock spectra. The solid profile shows a symmetric profile. The dashed profile shows an asymmetric profile. The blue and red colors represent the blueshift and redshift. (b) CoG for mock spectra. The colors and curves are coded the same as panel (a) and the black solid line is the total CoG of solid profile in panel (a). Purple and green lines mark the position of $F_{85}(V_{85})$ and $F_{25}(V_{25})$. (c) Mock spectra. The black, green and red profiles display flat-topped, single-peaked and double-horned shapes. (d) Normalized CoG for mock spectra. The colors and curves are coded the same as panel (c). The light-green area represents the K value for the single-peaked profile. The light-red area represents the absolute K value for the double-horned profile.

4.2. HI profiles in misaligned galaxies

Applying the CoG method to the HI spectra in misaligned galaxies and aligned controls, we can compare the shape of HI profile between them. Figure 7 displays the distributions of C_V . The blue and gray histograms in Figure 7(a) show the distributions for misaligned galaxies and aligned controls in SF sequence. The blue and gray bars on the top mark the corresponding median values. The SF misaligned galaxies have similar C_V distribution as their controls with a slightly higher median C_V

value. We perform a KS test on these distributions, which is a non-parametric method to quantify the difference between two distributions with p -value < 0.05 indicating a significant difference existing between two distributions. The KS test gives a p -value of 0.96 for the C_V distributions, which indicates that there is no significant difference in HI profiles between SF misaligned galaxies and aligned controls. The red and gray histograms in Figure 7(b) show the distributions of C_V for misaligned galaxies and aligned controls in QS sequence. The bars on the top mark the median values, color-coded in the same way as histograms. The C_V value in QS misaligned galaxies is obviously higher than that in QS aligned controls with a p -value of 0.03. This indicates that the confidence level of difference in C_V distributions between misaligned galaxies and the control sample reaches 97%, implying more concentrated HI profiles in QS misaligned galaxies than their controls.

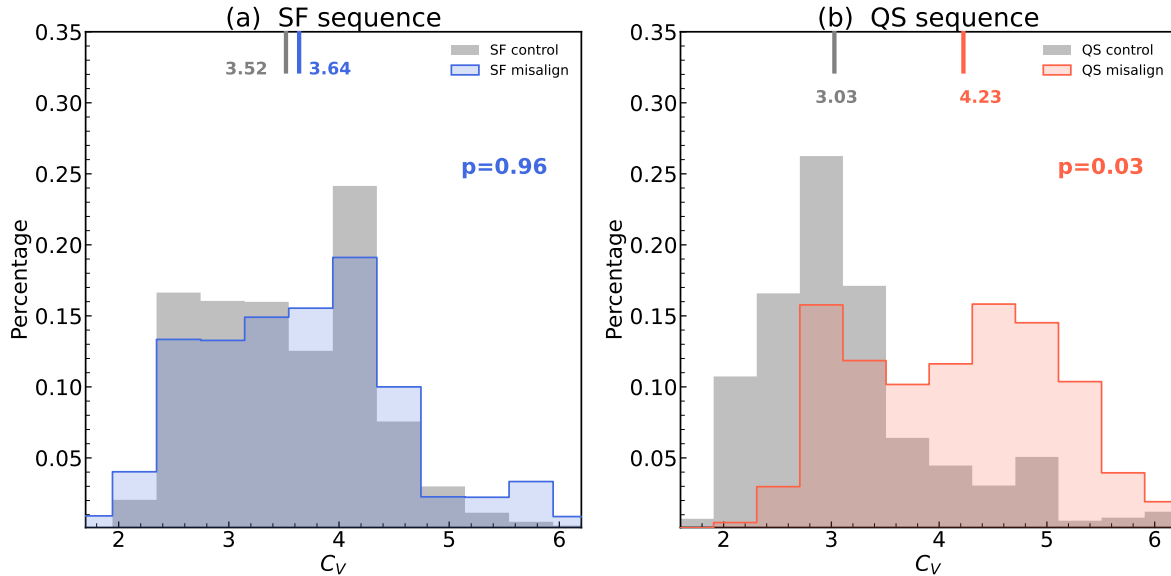


Figure 7. The distributions of C_V for misaligned galaxies and aligned controls. (a) The blue and gray histograms show the C_V distribution for SF misaligned galaxies and their aligned controls, respectively. The blue and gray bars on the top mark the corresponding median values. The p -value from KS test of this distribution is marked by blue text in the plot. (b) The red and gray histograms show the C_V distribution for QS misaligned galaxies and their aligned controls, respectively. The red and gray bars on the top mark the corresponding median values. The p -value from KS test of this distribution is marked by red text in the plot.

By definition, the two parameters K and C_V are physically related, with higher values of K & C_V indicating higher concentration of HI profiles. Since the calculation of parameter K makes use of the full information from the CoG, it can better quantify the HI spectral shape with a positive K value indicating a single-peaked HI profile and a negative K value indicating a double-horned HI profile. On the contrary, C_V , relying only on the ratio of two line widths, can only qualitatively measure the concentration of the spectrum. Figure 8 displays the distributions of K for misaligned galaxies and aligned controls, with colors and symbols coded in the same way as Figure 7. The vertical dashed line marks the position of $K = 0$, corresponding to a flat-topped shape. Figure 8(a) displays the K distributions for SF sequence. The SF misaligned galaxies have slightly higher median K value

than their controls with a p-value of 0.75. Figure 8(b) displays the distributions in QS sequence, where the difference in K between misaligned galaxies and aligned controls is significant. The K value for QS misaligned galaxies tends to be positive, indicating that the HI profiles in these galaxies are dominated by single-peaked profiles. Meanwhile, the K value for QS aligned controls tends to be negative, corresponding to double-horned profiles. KS test gives a p-value of 0.01, indicating that the distributions of parameter K between QS misaligned galaxies and the control sample are different at 99% confidence level. The HI profiles in QS misaligned galaxies are remarkably more concentrated than that in QS aligned controls.

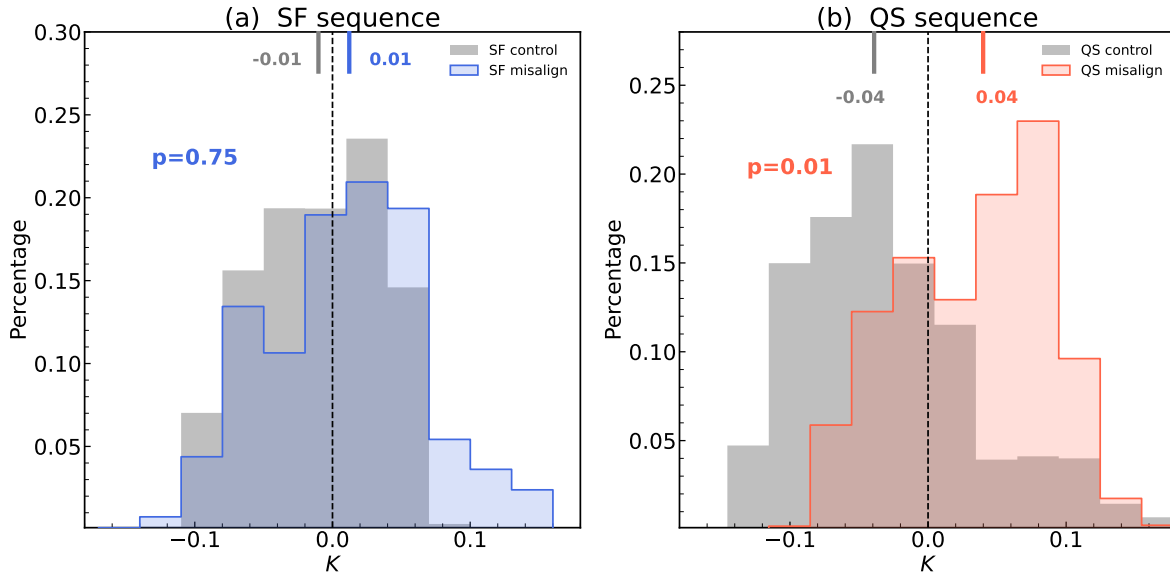


Figure 8. The distributions of K for misaligned galaxies and aligned controls. (a) The blue and gray histograms show the K distribution for SF misaligned galaxies and their aligned controls, respectively. The blue and gray bars on the top mark the corresponding median values. The p-value from KS test of this distribution is marked by blue text in the plot. (b) The red and gray histograms show the K distribution for QS misaligned galaxies and their aligned controls, respectively. The red and gray bars on the top mark the corresponding median values. The p-value from KS test of this distribution is marked by red text in the plot. In panels (a) & (b), the vertical dashed line marks the value of $K = 0$, corresponding to the flat-topped shape.

Figure 9 displays the distributions of the asymmetry parameter A_F , with colors and symbols coded in the same way as Figure 7. It is obvious that the difference in A_F distributions between misaligned galaxies and aligned controls can be neglected in both SF sequence (Figure 9a) and QS sequence (Figure 9b) with a p-value of 0.75 (0.83) for SF (QS) sequence. Although the HI spectra we analyzed are single-dish without any spatial resolution, the similar distributions of the parameter A_F in misaligned galaxies and their aligned controls imply the consistent spectral asymmetry of HI spectra in these galaxies and that external gas accretion does not lead to significant asymmetry in gas kinematics. Zhou et al. (2022) compared the asymmetry of the ionized gaseous velocity fields between misaligned galaxies and their aligned controls selected from the MaNGA survey, finding obviously higher asymmetry for misaligned galaxies in both SF sequence and QS sequence. The inconsistency

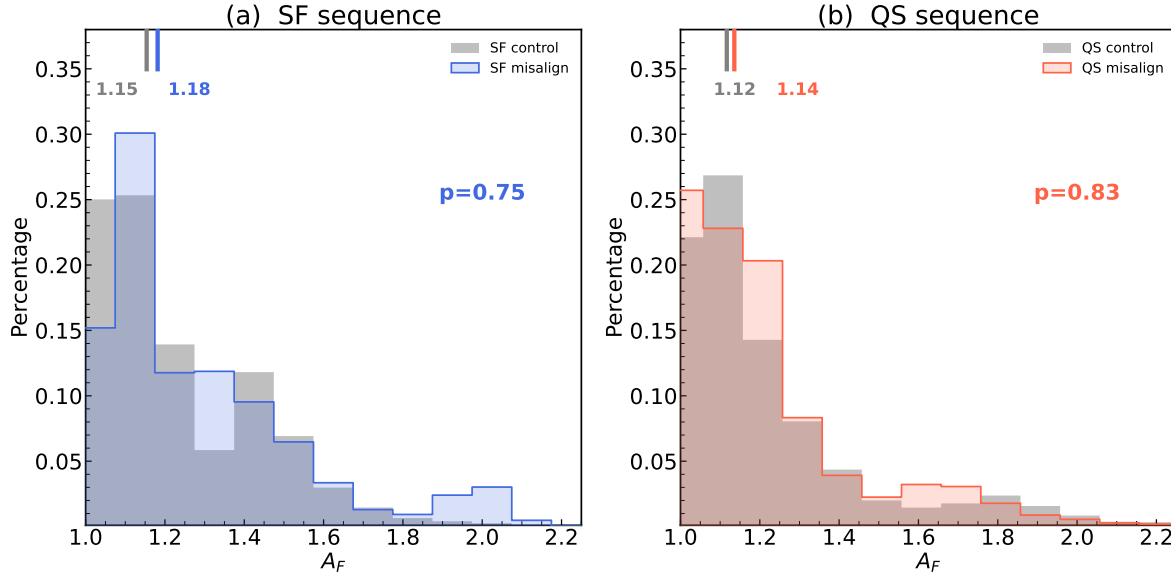


Figure 9. The distributions of A_F for misaligned galaxies and aligned controls. (a) The blue and gray histograms show the A_F distribution for SF misaligned galaxies and their aligned controls, respectively. The blue and gray bars on the top mark the corresponding median values. The p-value from KS test of this distribution is marked by blue text in the plot. (b) The red and gray histograms show the A_F distribution for QS misaligned galaxies and their aligned controls, respectively. The red and gray bars on the top mark the corresponding median values. The p-value from KS test of this distribution is marked by red text in the plot.

between the results from the current work and that from Zhou et al. (2022) might be due to that we study different gas-phases, H_I traced cold gas versus optical emission lines traced ionized gas in Zhou et al. (2022). Without further spatially resolved observations in H_I gas, we will not over-interpret this difference in asymmetry between different gas phases here.

5. IMPACT OF EXTERNAL GAS ACCRETION ON H_I PROFILE

The distributions of H_I line widths in misaligned galaxies and their aligned controls (shown in Figure 4) indicate that misaligned galaxies exhibit statistically narrower line widths compared with their aligned controls. Additionally, the C_V in Figure 7, a parameter traditionally used to indicate the spectral concentration, shows a consistent trend with the results for the superior parameter K in Figure 8. These findings, based on individual H_I line measurements, are consistent with the comparison of stacked spectra in Figure 5. On the one hand, for both SF sequence and QS sequence, the misaligned galaxies show higher K (or C_V) values, representing more concentrated H_I profiles. On the other hand, the difference in K (or C_V) values between misaligned galaxies and aligned controls is more prominent in QS sequence compared to the SF sequence, indicating more obvious influence of H_I gas accretion on QS misaligned galaxies than SF ones.

Previous works have done a lot of studies based on the optical spectra and suggested that the impact of external gas accretion on SF and QS misaligned galaxies is different. For SF misaligned galaxies, both Chen et al. (2016) and Jin et al. (2016) found lower D_n4000 (younger stellar population) and higher sSFR in the central regions than their outskirts. Xu et al. (2022) found positive D_n4000

gradients in SF misaligned galaxies while negative gradients in aligned controls. These results can be explained by a picture that the progenitors of SF misaligned galaxies accrete misaligned gas from gas-rich dwarfs or cosmic web. The interaction between accreted gas and pre-existing gas leads to the re-distribution of angular momentum, causing large amount of gas inflow and triggering the central star formation. For QS galaxies, the lack of difference in stellar population gradients between misaligned galaxies and aligned controls is due to that the progenitors of QS misaligned galaxies are gas-poor, the angular momentum loss mechanism described above does not exist in the QS misaligned galaxies (Zhou et al. 2022).

Based on this picture, we would expect that the difference in HI spectral shape should be more apparent in SF misaligned galaxies and their aligned controls. However, our observational results clearly show significant HI spectral shape differences in QS misaligned galaxies and their aligned controls, the difference is not obvious in SF misaligned galaxies and their aligned controls. To understand this result, we simulate variations of the K values measured by the CoG method for galaxies with different HI surface density distributions. Figure 10(a) displays the mimic HI surface density (Σ_{HI}) profiles, which can be described as segmented functions. For $r < 0.7R_{\text{HI}}$, $\Sigma_{\text{HI}} \propto -s(R/R_{\text{HI}}) + b$, with R_{HI} representing the radius of a galaxy where averaged $\Sigma_{\text{HI}} \sim 1 M_{\odot}/\text{pc}^2$. The s values ranging from negative (central HI-deficient) to positive (central HI-enriched) corresponds to the profiles from red to purple, as shown in the colorbar of Figure 10 (a). At $r > 0.7R_{\text{HI}}$, Σ_{HI} is described as an exponential decline function $\Sigma_{\text{HI}} \propto e^{-R/R_{\text{HI}}}$ (Wang et al. 2016). Combining the Σ_{HI} profiles with a uniform rotation curve, we can have the HI emission profile models. In Figure 10(b) we show the normalized CoG measured from HI emission profile models and the derived K in Figure 10(c). Different colors in Figure 10(b) and (c) are corresponds to different Σ_{HI} profiles shown in Figure 10(a). As shown in Figure 10(c), the dependence of K on s can be described by a double power law. For $s < 0$, K increases with s very quickly, namely, as a galaxy transits from central HI-deficient to central HI-enriched (from red curve to cyan curve in Figure 10a), its spectrum changes from double-horned to single-peaked shape, accompanied by a significant increase in K value from negative to positive. However, at $s > 0$, the dependence weakens, K increases slowly with s , namely, once the galaxy is already central HI-enriched (from cyan curve to purple curve in Figure 10a), further increases in central HI density will not have strong impact on measured K values. Wang et al. (2016) compared the radial gradients of Σ_{HI} in different types of galaxies, and found that early-type galaxies have lower Σ_{HI} in the inner region, whereas spiral galaxies show an exponential decline of Σ_{HI} radial profile. Bigiel et al. (2008) identified a universal saturation threshold ($\Sigma_{\text{HI}} \sim 9 M_{\odot}/\text{pc}^2$) for atomic hydrogen (HI) surface density. They suggest that HI gas is effectively converted into H₂ at $\Sigma_{\text{HI}} > 9 M_{\odot}/\text{pc}^2$, providing fuel for the formation of new stars. This saturation is observed in galactic centers, outskirts, and dwarf galaxies. As a consequence, the difference in K and C_V between misaligned galaxies and their aligned controls can be explained in the following ways:

1. The progenitors of SF misaligned galaxies have central enriched HI ($s > 0$), which leads to single-peaked HI emission profiles. The interaction between accreted HI and pre-existing HI redistributes the AM of HI gas, inducing gas inflow (as suggested by Chen et al. 2016). However, the lack of obvious difference in K and C_V values between misaligned galaxies and their aligned controls is due to the insensitivity of K and C_V on Σ_{HI} gradient at $s > 0$ (as simulated in Figure 10). Another possible scenario is that the inflowing HI gas in SF misaligned galaxies is

converted into molecular gas and trigger star formation, preventing significant increase of HI gas surface density in their central regions.

2. The progenitors of QS misaligned galaxies are dominated by early-type galaxies, they are initially central HI-deficient ($s < 0$) with double-horned HI profiles. On the one hand, the interaction between the accreted HI and the pre-existing HI leads to the re-distribution of gas AM and induces gas inflow, replenishing central HI reservoirs. The transition from central HI deficiency to sufficiency—a ‘from-scratch’ replenishment process—causes a significant increase in K or C_V values for misaligned galaxies. On the other hand, although these QS misaligned galaxies have undergone cold gas inflow processes, the HI gas surface densities in their central regions remain below the critical threshold ($\sim 9 M_\odot/\text{pc}^2$) required for HI-H₂ transition. This is consistent with the results from optical observations in Zhou et al. (2022), where they did not find any new formed stars in the QS misaligned galaxies.

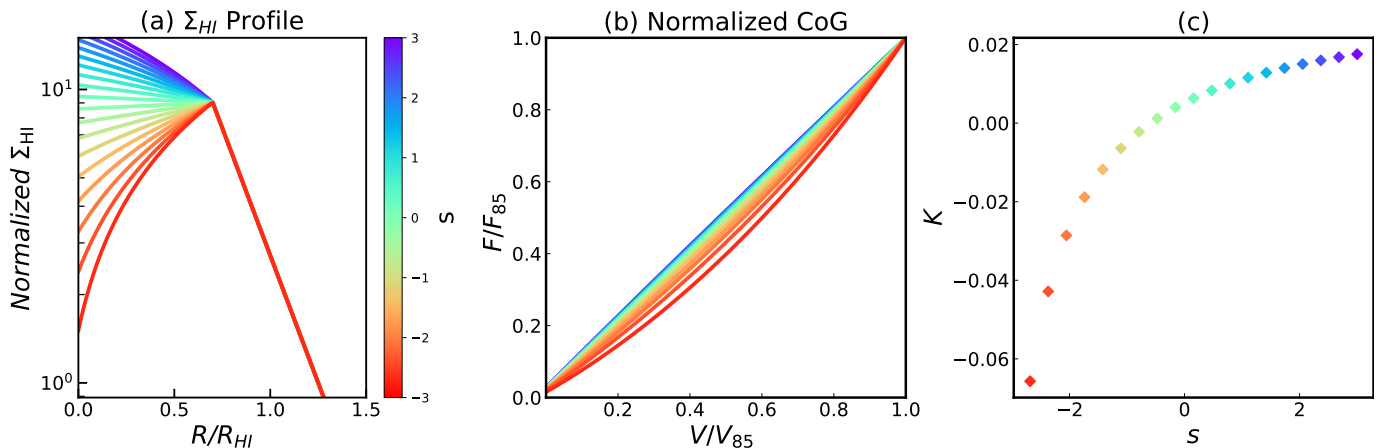


Figure 10. The variations of the K values with different HI surface density profiles. (a) HI surface density profiles, with the colorbar showing the s values. From bottom to top, the HI surface density at the center of the galaxy goes from deficient to enriched responding from the red to the purple solid lines. (b) The normalized CoG obtained from the spectra corresponding to each HI surface density distribution in panel (a) with all other parameters fixed, and the area enclosed by the CoG and the diagonal line is the corresponding K value with the color-coded in the same way as panel (a). (c) Relationship between HI surface density profiles and K values. s represents the slope of HI surface density in galactic center with a larger s indicating a higher central HI surface density. The color-code is in the same way as panel (a).

6. CONCLUSION

In this study, we build a sample of 37 gas-star misaligned galaxies with robust HI observations from the final data release of the MaNGA. To explore the impact of external gas accretion on the HI distribution, we construct a control sample of aligned galaxies with similar stellar mass, D_n4000 and inclination angle as well as robust HI measurement. We also classify the misaligned galaxies and aligned controls into star-forming (SF) sequence and quiescent (QS) sequence to investigate the impact separately. The main observational results are as follows:

1. The stacked HI spectra in misaligned galaxies are narrower in line width than their aligned controls in SF sequence and QS sequence. The difference in line width is more obvious in the QS sequence.
2. The median C_V and K values in SF misaligned galaxies are slightly higher than SF aligned controls, while the distributions of them are comparable. The C_V and K distributions in QS misaligned galaxies are prominently higher than QS align controls, with HI spectra are dominated by single-peaked shapes in the misaligned galaxies and double-horned shapes in the aligned controls.
3. The difference in HI spectral asymmetry between misaligned galaxies and aligned controls can be neglected in both SF sequence and QS sequence. Without further spatially resolved observations in HI, we will not over-interpret this difference in this work.

The difference in spectral shape of misaligned galaxies and their aligned controls suggests that the interaction between the external accreted gas and the pre-existing gas leads to the re-distribution of gas angular momentum and induces gas inflow. The progenitors of SF misaligned galaxies are central HI-enriched. In this case, the measured K value is not sensitive to the increase of central HI surface density. On the other hand, as the HI surface density increases to $\sim 9 M_\odot/\text{pc}^2$, the HI-H₂ transition happens, preventing significant increase of HI gas surface density in their central regions. The progenitors of QS misaligned galaxies are central HI-deficient with double-horned HI profiles. The transition from central HI-deficient to central HI-enriched through external gas accretion results in a significant increase in K or C_V values for misaligned galaxies. Although these QS misaligned galaxies have undergone cold gas inflow processes, the central HI gas surface densities fail to reach the critical threshold for HI-H₂ transition ($\sim 9 M_\odot/\text{pc}^2$). This finding agrees with the results from optical observations in Zhou et al. (2022), which found no evidence of newly formed stars in QS misaligned galaxies.

Acknowledgements: MB acknowledges support by the National Natural Science Foundation of China, NSFC Grant no. 12303009. YMC acknowledges support by the National Natural Science Foundation of China, NSFC Grant no. 12333002 and the China Manned Space Project, no. CMS-CSST-2025-A08. LCH was supported by the National Science Foundation of China, NSFC Grant no. 12233001 and the National Key R&D Program of China (2022YFF0503401). NKY acknowledges support by the projects funded by China Postdoctoral Science Foundation no. 2022M723175 and GZB20230766.

Funding for the Sloan Digital Sky Survey IV has been provided by the Alfred P. Sloan Foundation, the U.S. Department of Energy Office of Science, and the Participating Institutions. SDSS-IV acknowledges support and resources from the Center for High-Performance Computing at the University of Utah. The SDSS web site is www.sdss.org. SDSS-IV is managed by the Astrophysical Research Consortium for the Participating Institutions of the SDSS Collaboration including the Brazilian Participation Group, the Carnegie Institution for Science, Carnegie Mellon University, the Chilean Participation Group, the French Participation Group, Harvard-Smithsonian Center for Astrophysics, Instituto de Astrofísica de Canarias, The Johns Hopkins University, Kavli Institute for the Physics and Mathematics of the Universe (IPMU) / University of Tokyo, Lawrence Berkeley National Laboratory, Leibniz Institut für Astrophysik Potsdam (AIP), Max-Planck-Institut für Astronomie (MPIA Heidelberg), Max-Planck-Institut für Astrophysik (MPA Garching), Max-Planck-Institut für

Extraterrestrische Physik (MPE), National Astronomical Observatory of China, New Mexico State University, New York University, University of Notre Dame, Observatório Nacional / MCTI, The Ohio State University, Pennsylvania State University, Shanghai Astronomical Observatory, United Kingdom Participation Group, Universidad Nacional Autónoma de México, University of Arizona, University of Colorado Boulder, University of Oxford, University of Portsmouth, University of Utah, University of Virginia, University of Washington, University of Wisconsin, Vanderbilt University, and Yale University.

REFERENCES

Abdurro'uf, Accetta, K., Aerts, C., et al. 2022, ApJS, 259, 35, doi: [10.3847/1538-4365/ac4414](https://doi.org/10.3847/1538-4365/ac4414)

Bao, M., Chen, Y., Gu, Q., et al. 2025, ApJL, 982, L29, doi: [10.3847/2041-8213/adbc68](https://doi.org/10.3847/2041-8213/adbc68)

Barrera-Ballesteros, J. K., García-Lorenzo, B., Falcón-Barroso, J., et al. 2015, A&A, 582, A21, doi: [10.1051/0004-6361/201424935](https://doi.org/10.1051/0004-6361/201424935)

Bigiel, F., Leroy, A., Walter, F., et al. 2008, AJ, 136, 2846, doi: [10.1088/0004-6256/136/6/2846](https://doi.org/10.1088/0004-6256/136/6/2846)

Blanton, M. R., Kazin, E., Muna, D., Weaver, B. A., & Price-Whelan, A. 2011, AJ, 142, 31, doi: [10.1088/0004-6256/142/1/31](https://doi.org/10.1088/0004-6256/142/1/31)

Blanton, M. R., & Roweis, S. 2007, AJ, 133, 734, doi: [10.1086/510127](https://doi.org/10.1086/510127)

Blanton, M. R., Bershady, M. A., Abolfathi, B., et al. 2017, AJ, 154, 28, doi: [10.3847/1538-3881/aa7567](https://doi.org/10.3847/1538-3881/aa7567)

Bruzual, G., & Charlot, S. 2003, MNRAS, 344, 1000, doi: [10.1046/j.1365-8711.2003.06897.x](https://doi.org/10.1046/j.1365-8711.2003.06897.x)

Bryant, J. J., Croom, S. M., van de Sande, J., et al. 2019, MNRAS, 483, 458, doi: [10.1093/mnras/sty3122](https://doi.org/10.1093/mnras/sty3122)

Bundy, K., Bershady, M. A., Law, D. R., et al. 2015, ApJ, 798, 7, doi: [10.1088/0004-637X/798/1/7](https://doi.org/10.1088/0004-637X/798/1/7)

Chabrier, G. 2003, PASP, 115, 763, doi: [10.1086/376392](https://doi.org/10.1086/376392)

Chen, Y.-M., Shi, Y., Tremonti, C. A., et al. 2016, Nature Communications, 7, 13269, doi: [10.1038/ncomms13269](https://doi.org/10.1038/ncomms13269)

Corsini, E. M. 2014, in Astronomical Society of the Pacific Conference Series, Vol. 486, Multi-Spin Galaxies, ed. E. Iodice & E. M. Corsini, 51, doi: [10.48550/arXiv.1403.1263](https://doi.org/10.48550/arXiv.1403.1263)

Davis, T. A., Alatalo, K., Sarzi, M., et al. 2011, MNRAS, 417, 882, doi: [10.1111/j.1365-2966.2011.19355.x](https://doi.org/10.1111/j.1365-2966.2011.19355.x)

Duckworth, C., Starkenburg, T. K., Genel, S., et al. 2020a, MNRAS, 495, 4542, doi: [10.1093/mnras/staa1494](https://doi.org/10.1093/mnras/staa1494)

Duckworth, C., Tojeiro, R., & Kraljic, K. 2020b, MNRAS, 492, 1869, doi: [10.1093/mnras/stz3575](https://doi.org/10.1093/mnras/stz3575)

El-Badry, K., Bradford, J., Quataert, E., et al. 2018, MNRAS, 477, 1536, doi: [10.1093/mnras/sty730](https://doi.org/10.1093/mnras/sty730)

Fabollo, S., Kauffmann, G., Catinella, B., et al. 2012, MNRAS, 427, 2841, doi: [10.1111/j.1365-2966.2012.22088.x](https://doi.org/10.1111/j.1365-2966.2012.22088.x)

Galletta, G. 1987, ApJ, 318, 531, doi: [10.1086/165389](https://doi.org/10.1086/165389)

Gunn, J. E., Siegmund, W. A., Mannery, E. J., et al. 2006, AJ, 131, 2332, doi: [10.1086/500975](https://doi.org/10.1086/500975)

Haynes, M. P., Giovanelli, R., Kent, B. R., et al. 2018, ApJ, 861, 49, doi: [10.3847/1538-4357/aac956](https://doi.org/10.3847/1538-4357/aac956)

Jin, Y., Chen, Y., Shi, Y., et al. 2016, MNRAS, 463, 913, doi: [10.1093/mnras/stw2055](https://doi.org/10.1093/mnras/stw2055)

Kennicutt, R. C., & Evans, N. J. 2012, ARA&A, 50, 531, doi: [10.1146/annurev-astro-081811-125610](https://doi.org/10.1146/annurev-astro-081811-125610)

Kornreich, D. A., Haynes, M. P., Lovelace, R. V. E., & van Zee, L. 2000, AJ, 120, 139, doi: [10.1086/301422](https://doi.org/10.1086/301422)

Krajnović, D., Cappellari, M., de Zeeuw, P. T., & Copin, Y. 2006, MNRAS, 366, 787, doi: [10.1111/j.1365-2966.2005.09902.x](https://doi.org/10.1111/j.1365-2966.2005.09902.x)

Lagos, C. d. P., Padilla, N. D., Davis, T. A., et al. 2015, MNRAS, 448, 1271, doi: [10.1093/mnras/stu2763](https://doi.org/10.1093/mnras/stu2763)

Law, D. R., Cherinka, B., Yan, R., et al. 2016, AJ, 152, 83, doi: [10.3847/0004-6256/152/4/83](https://doi.org/10.3847/0004-6256/152/4/83)

L’Huillier, B., Combes, F., & Semelin, B. 2012, A&A, 544, A68, doi: [10.1051/0004-6361/201117924](https://doi.org/10.1051/0004-6361/201117924)

Li, S.-l., Shi, Y., Bizyaev, D., et al. 2021, MNRAS, 501, 14, doi: [10.1093/mnras/staa3618](https://doi.org/10.1093/mnras/staa3618)

Lu, S., Xu, D., Wang, Y., et al. 2021, MNRAS, 503, 726, doi: [10.1093/mnras/stab497](https://doi.org/10.1093/mnras/stab497)

Masters, K. L., Stark, D. V., Pace, Z. J., et al. 2019, MNRAS, 488, 3396, doi: [10.1093/mnras/stz1889](https://doi.org/10.1093/mnras/stz1889)

Reichard, T. A., Heckman, T. M., Rudnick, G., Brinchmann, J., & Kauffmann, G. 2008, ApJ, 677, 186, doi: [10.1086/526506](https://doi.org/10.1086/526506)

Sarzi, M., Falcón-Barroso, J., Davies, R. L., et al. 2006, MNRAS, 366, 1151, doi: [10.1111/j.1365-2966.2005.09839.x](https://doi.org/10.1111/j.1365-2966.2005.09839.x)

Stark, D. V., Masters, K. L., Avila-Reese, V., et al. 2021, MNRAS, 503, 1345, doi: [10.1093/mnras/stab566](https://doi.org/10.1093/mnras/stab566)

Wang, J., Koribalski, B. S., Serra, P., et al. 2016, MNRAS, 460, 2143, doi: [10.1093/mnras/stw1099](https://doi.org/10.1093/mnras/stw1099)

Wang, J., Lin, X., Yang, D., et al. 2024, ApJ, 968, 48, doi: [10.3847/1538-4357/ad3e61](https://doi.org/10.3847/1538-4357/ad3e61)

Westfall, K. B., Cappellari, M., Bershady, M. A., et al. 2019, AJ, 158, 231, doi: [10.3847/1538-3881/ab44a2](https://doi.org/10.3847/1538-3881/ab44a2)

Witherspoon, C. A., & Wilcots, E. M. 2024, ApJ, 961, 192, doi: [10.3847/1538-4357/acfc8](https://doi.org/10.3847/1538-4357/acfc8)

Xu, H., Chen, Y., Shi, Y., et al. 2022, MNRAS, 511, 4685, doi: [10.1093/mnras/stac354](https://doi.org/10.1093/mnras/stac354)

Yu, N., Ho, L. C., & Wang, J. 2020, ApJ, 898, 102, doi: [10.3847/1538-4357/ab9ac5](https://doi.org/10.3847/1538-4357/ab9ac5)

Yu, N., Ho, L. C., Wang, J., & Li, H. 2022, ApJS, 261, 21, doi: [10.3847/1538-4365/ac626b](https://doi.org/10.3847/1538-4365/ac626b)

Yun, M. S., Ho, P. T. P., & Lo, K. Y. 1994, Nature, 372, 530, doi: [10.1038/372530a0](https://doi.org/10.1038/372530a0)

Zhou, Y., Chen, Y., Shi, Y., et al. 2022, MNRAS, 515, 5081, doi: [10.1093/mnras/stac2016](https://doi.org/10.1093/mnras/stac2016)